

Hybrid molecular beam epitaxy for the growth of stoichiometric BaSnO₃

Abhinav Prakash, John Dewey, Hwanhui Yun, Jong Seok Jeong, K. Andre Mkhoyan, and Bharat Jalan

Citation: *Journal of Vacuum Science & Technology A* **33**, 060608 (2015); doi: 10.1116/1.4933401

View online: <http://dx.doi.org/10.1116/1.4933401>

View Table of Contents: <http://scitation.aip.org/content/avs/journal/jvsta/33/6?ver=pdfcov>

Published by the AVS: Science & Technology of Materials, Interfaces, and Processing

Articles you may be interested in

[Growth of SrVO₃ thin films by hybrid molecular beam epitaxy](#)

J. Vac. Sci. Technol. A **33**, 061504 (2015); 10.1116/1.4927439

[Impurity distribution and microstructure of Ga-doped ZnO films grown by molecular beam epitaxy](#)

J. Appl. Phys. **112**, 123527 (2012); 10.1063/1.4769801

[Molecular beam epitaxial growth of BaTiO₃ single crystal on Ge-on-Si\(001\) substrates](#)

Appl. Phys. Lett. **98**, 092901 (2011); 10.1063/1.3558997

[Epitaxial growth of \(001\)-oriented Ba_{0.5}Sr_{0.5}TiO₃ thin films on a -plane sapphire with an MgO/ZnO bridge layer](#)


Appl. Phys. Lett. **95**, 212901 (2009); 10.1063/1.3266862

[Epitaxial growth and strain relaxation of BaTiO₃ thin films on SrTiO₃ buffered \(001\) Si by molecular beam epitaxy](#)

J. Vac. Sci. Technol. B **25**, 1053 (2007); 10.1116/1.2539503



Instruments for Advanced Science

<p>Contact Hiden Analytical for further details: W www.HidenAnalytical.com E info@hiden.co.uk</p> <p>CLICK TO VIEW our product catalogue</p>	 <p>Gas Analysis</p> <ul style="list-style-type: none"> › dynamic measurement of reaction gas streams › catalysis and thermal analysis › molecular beam studies › dissolved species probes › fermentation, environmental and ecological studies 	 <p>Surface Science</p> <ul style="list-style-type: none"> › UHV TPD › SIMS › end point detection in ion beam etch › elemental imaging - surface mapping 	 <p>Plasma Diagnostics</p> <ul style="list-style-type: none"> › plasma source characterization › etch and deposition process reaction › kinetic studies › analysis of neutral and radical species 	 <p>Vacuum Analysis</p> <ul style="list-style-type: none"> › partial pressure measurement and control of process gases › reactive sputter process control › vacuum diagnostics › vacuum coating process monitoring
---	--	--	--	--

Hybrid molecular beam epitaxy for the growth of stoichiometric BaSnO₃

Abhinav Prakash,^{a)} John Dewey, Hwanhui Yun, Jong Seok Jeong, K. Andre Mkhoyan, and Bharat Jalan^{b)}

Department of Chemical Engineering and Materials Science, University of Minnesota, Minneapolis, Minnesota 55455

(Received 22 September 2015; accepted 6 October 2015; published 19 October 2015)

Owing to its high room-temperature electron mobility and wide bandgap, BaSnO₃ has recently become of significant interest for potential room-temperature oxide electronics. A hybrid molecular beam epitaxy (MBE) approach for the growth of high-quality BaSnO₃ films is developed in this work. This approach employs hexamethylditin as a chemical precursor for tin, an effusion cell for barium, and a radio frequency plasma source for oxygen. BaSnO₃ films were thus grown on SrTiO₃ (001) and LaAlO₃ (001) substrates. Growth conditions for stoichiometric BaSnO₃ were identified. Reflection high-energy electron diffraction (RHEED) intensity oscillations, characteristic of a layer-by-layer growth mode were observed. A critical thickness of ~1 nm for strain relaxation was determined for films grown on SrTiO₃ using *in situ* RHEED. Scanning transmission electron microscopy combined with electron energy-loss spectroscopy and energy dispersive x-ray spectroscopy confirmed the cube-on-cube epitaxy and composition. The importance of precursor chemistry is discussed in the context of the MBE growth of BaSnO₃. © 2015 American Vacuum Society.

[<http://dx.doi.org/10.1116/1.4933401>]

I. INTRODUCTION

Choice of synthesis conditions for a metal oxide are often informed by thermodynamics considerations, as commonly represented in the Ellingham diagram. Consideration of the metal's redox potential can also be instructive. Metals possessing high oxidation potential are readily oxidized, whereas those with lower potential require stronger reaction conditions: high oxygen pressures,¹ high processing temperatures,^{2,3} sol-gel chemistry,^{4,5} application of reactive gases such as ozone,^{6–11} or even combustion.¹² For ternary oxides such as perovskite oxides (ABO₃, where A and B are elemental metals), a difference in oxidation potentials of metal A and B can make synthesis even more demanding as compared to their binary oxide counterparts. For instance, if metal B has a lower oxidation potential than that of metal A, a more severe oxidation condition may be required to achieve full oxidation of B in the presence of A. Figure 1 shows the standard oxidation potential^{13,14} of elements used in common perovskite oxides. B-site elements (Ti, V, Sn, Ni, etc.), in general, have lower oxidation potential than A-site elements (Ba, Sr, La, Y, etc.), implying stronger oxidation conditions may be required for nickelates or stannates as compared to their titanate equivalents. Owing to this complication, ultra-high vacuum (UHV) growth techniques such as oxide molecular beam epitaxy (MBE) often result in incomplete oxidation of elements with low oxidation potential, leading to the formation of secondary phases. For example, NiO is a known impurity phase in nickelates due to incomplete oxidation of Ni under standard MBE conditions.¹⁵ Similarly, undesirable SnO phase forms during the MBE growth of SnO₂.¹⁶ Potentially, higher oxygen pressure or the application of reactive gases such as hydrogen

peroxide¹⁷ or ozone^{6–11} can be used to avoid such issues. However, they may lead to undesirable consequences in MBE such as metal flux instability^{18–20} due to the surface oxidation, or filament oxidation, or even damage to the vacuum pumps due to high oxygen pressure.

Alternative MBE approaches, such as hybrid MBE, overcome these challenges to a certain extent.^{21,22} Hybrid MBE supplies low-vapor-pressure-elements in the form of chemical precursors, with metal atoms already bound to oxygen.

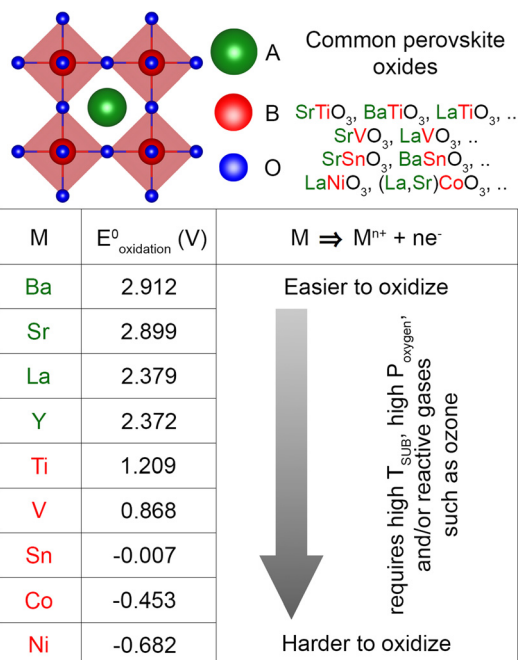


Fig. 1. (Color online) Standard oxidation potentials for A- and B-site elements in common perovskite oxides, ABO₃ in the order of increasing difficulty to oxidize them to their respective oxidation state. For these values, note that n = 2 for Ba and Sr; n = 3 for La, Y, Ti, V, Co, and Ni; n = 4 for Sn. Data were taken from Refs. 13 and 14.

^{a)}Electronic mail: praka019@umn.edu

^{b)}Electronic mail: bjalan@umn.edu

For example, titanium tetraisopropoxide^{23–25} (TTIP) and vanadium oxytriisopropoxide^{26,27} (VTIP) precursors are used to supply Ti and V, respectively. The advantages of this approach include scalable growth rates, self-regulating stoichiometry control,^{23–25} and potentially superior oxygen stoichiometry owing to the additional source of oxygen from the precursor. However, it may not always be possible to find an oxygen-containing metal precursor that benefits the oxide growth in this fashion. In particular, for the stannate compounds (ASnO_3), identifying a suitable precursor is non-trivial. Emulating the recent success of TTIP (Refs. 23–25) and VTIP (Refs. 26, and 27) precursors, a chemical precursor like tin *tert*-butoxide (TTB)²⁸ that coordinates tin atoms to four oxygen atoms would appear to be a logical choice. When tested, however, TTB was found to be thermally unstable, with a vapor pressure much lower than appropriate²⁹ for use in the MBE system.

In this letter, we report on a hybrid MBE approach for epitaxial growth of phase-pure, stoichiometric BaSnO_3 films using hexamethylditin, $(\text{CH}_3)_6\text{Sn}_2$ (HMDT) as a tin precursor. It is noteworthy that the reactivity of HMDT is strong enough to produce phase-pure BaSnO_3 films when combined not only with an oxygen plasma but also with molecular oxygen [see Fig. S1 (Ref. 30)]. Attempts to grow BaSnO_3 films using tetraethyltin (C_2H_5)₄Sn (TET), a similar alkyl-tin precursor²⁹ proven successful in the hybrid MBE growth of SnO_2 ,²⁹ resulted in drastically lower Sn incorporation [see Fig. S2 (Ref. 30)], even though growth conditions were kept identical. To the best of our knowledge, this is the first report on the MBE growth of BaSnO_3 .

II. EXPERIMENT

Phase-pure, single-crystalline, epitaxial BaSnO_3 (Refs. 31–33) films ($a_0 = 4.116 \text{ \AA}$; space group: $Pm\bar{3}m$) were grown by co-deposition on SrTiO_3 (STO) (001) and LaAlO_3 (LAO) (001) substrates in a UHV oxide MBE system (EVO 50, Omicron Nanotechnology, Germany). The lattice mismatch of BaSnO_3 is -5.12% and -7.89% (compressive) with SrTiO_3 and LaAlO_3 , respectively. A hybrid MBE approach was employed using HMDT (Sigma Aldrich, USA) as a metalorganic precursor for Sn, an elemental solid source for Ba using an effusion cell and an rf plasma source for oxygen. The plasma source (Mantis, UK), equipped with charge deflection plates, was operated at 250 W and oxygen pressure of 5×10^{-6} Torr. The HMDT precursor was introduced via a gas injector (E-Science, Inc., USA) by thermal evaporation in a bubbler, which was connected to the gas injector through a gas inlet system equipped with a linear leak valve and a Baratron manometer. The HMDT flux was controlled by feedback control of the linear leak valve. Given the high volatility of HMDT at low temperatures, no carrier gas was used. A 350-nm-thick Ta layer was deposited on the back of the substrates to improve heat transfer between the film and the substrate heater. Substrates were cleaned in oxygen plasma for 20 min prior to film deposition ensuring no carbon contamination was present at the surface. The growth of stoichiometric BaSnO_3 films was then carried out at a fixed substrate

temperature, 900°C (thermocouple temperature) for 1 h keeping the beam equivalent pressures for Sn and Ba at 1.3×10^{-6} and 5.0×10^{-8} Torr, respectively. Oxygen plasma was left on during cooling until the samples reached 400°C .

Film growth was monitored *in situ* using reflection high-energy electron diffraction (RHEED, Staib Instruments, Germany), operating at an accelerating voltage of 14 kV. Structural characterization was performed using a high-resolution Panalytical X'Pert thin-film diffractometer with Cu K_α radiation. Wide-angle x-ray diffraction (WAXRD) 2θ - ω scans and reciprocal space maps (RSMs) were taken to determine phase purity, and out-of-plane/in-plane lattice parameters. Grazing-incidence x-ray reflectivity (GIXR) scans, wide-angle x-ray diffraction finite-size fringes, and RHEED intensity oscillations were analyzed to determine the film's thicknesses, which were in excellent agreement with each other. GenX³⁴ was used to fit GIXR data. During film growth, time-dependent in-plane lattice parameters of BaSnO_3 were determined by measuring the spacing between diffraction streaks in real-time RHEED patterns, and then normalizing with respect to the spacing corresponding to the in-plane lattice parameter of the SrTiO_3 substrate [see Fig. S3 (Ref. 30)]. Atomic force microscopy (AFM) in contact mode was used to probe surface morphology. Scanning transmission electron microscopy (STEM) analysis was conducted using an aberration-corrected FEI Titan G2 60-300 STEM microscope equipped with a CEOS DCOR probe corrector operated at 200 keV. Energy dispersive x-ray spectroscopy (EDX) and electron energy-loss spectroscopy (EELS) maps were recorded using Super-X system with a quad-Silicon Drift Detector windowless in-polepiece EDX detector, and Gatan Enfinium ER spectrometer in the microscope, respectively. The convergent semiangle of the incident STEM probe beam was 21 mrad and the annular dark-field (ADF) detector inner angles were in the range of 43–77 mrad. Beam currents of 45 and 125 pA were used for imaging and spectroscopy, respectively. Transport measurement was performed using a Quantum Design physical property measurement system. Indium was used as an ohmic contact. No measurable conductivity ($<10^{-4} \Omega^{-1}\text{cm}^{-1}$) was observed in as-grown stoichiometric BaSnO_3 films.

III. RESULTS AND DISCUSSION

Figure 2(a) shows time-dependent RHEED intensity oscillations observed during a stoichiometric film growth. RHEED intensity oscillations indicate a two-dimensional Frank–van der Merwe (layer-by-layer) growth mode. A damping of the RHEED intensity for the first few monolayers was observed, which is attributed to an increase in the long-range roughness.^{35,36} However, a phase shift in the RHEED oscillations after 2–3 monolayers was observed, accompanied by an increase in the overall RHEED intensity. Such phase shifts are indicative of changes in growth dynamics and/or surface reconfiguration.^{37,38} In fact, we found that this abrupt phase shift is marked by the onset of strain relaxation as illustrated in Fig. 2(b), which shows time-dependent in-plane lattice parameters determined from

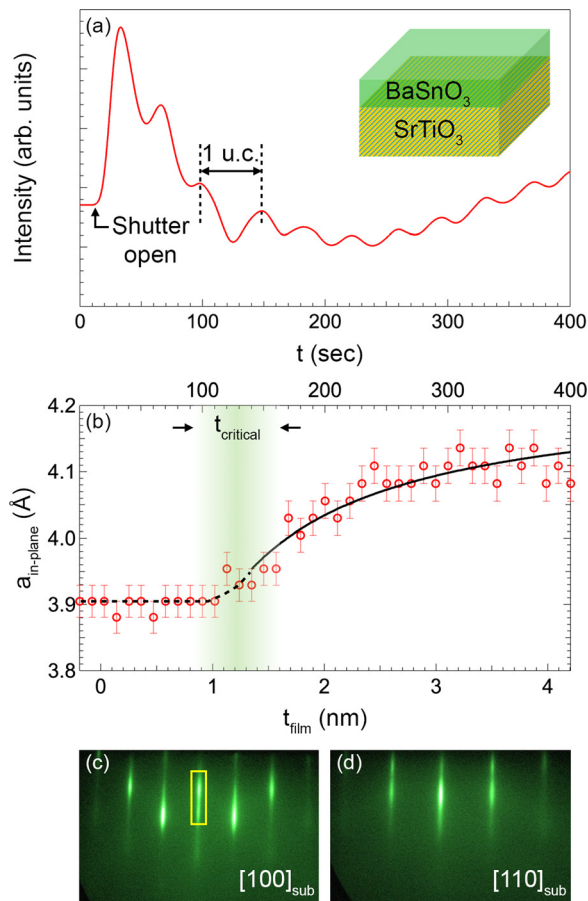


FIG. 2. (Color online) (a) Time-dependent RHEED intensity oscillations for BaSnO₃ grown on SrTiO₃ substrate. Inset shows the schematic of the structure. (b) In-plane lattice parameter of the film determined using *in situ* RHEED as a function of growth time. The shaded region marks the onset of strain relaxation. A black solid line above $t_{\text{film}} = 1.2$ nm is a hyperbolic fit to the experimental data. The dotted line is a guide to the eye. RHEED patterns after growth along (c) [100] and (d) [110] azimuths of the substrate. The film thickness is 40 nm.

the analysis of RHEED patterns [see Fig. S3 (Ref. 30)]. To obtain further insights into the mechanisms of strain relaxation, we analyzed the thickness-dependent (i.e., growth time-dependent) in-plane lattice parameters using the elastic theory of strain relaxation.³⁹ Figure 2(b) shows a reasonable fit (shown as a solid line) of the experimental data with a hyperbolic function, which represents strain relaxation behavior often via formation of misfit dislocations.³⁹ It is noted that our experimental critical thickness for strain relaxation (t_{critical}), ~ 1 nm, is smaller than the theoretical critical thickness value (~ 3 nm on SrTiO₃ substrate) determined using the Matthews–Blakeslee equation.⁴⁰ It should however be noted that the role of thermal stresses between film and substrate is not accounted for in the Matthews–Blakeslee equation, which may also be at play at high growth temperatures. After film growth, RHEED showed streaky patterns along both [100] and [110] azimuths of the substrate, establishing a cube-on-cube epitaxial relationship and smooth surface morphology [see Fig. S4 (Ref. 30)]. Further study is required, however, to understand the correlation between strain relaxation, phase shift, and growth dynamics.

The lattice parameter was used as a sensitive probe of the cation stoichiometry of our films. Figure 3(a) shows a WAXRD scan for a 40-nm-thick film on SrTiO₃ (001) with finite-size fringes, indicating crystalline phase and smooth morphology on a short lateral length scale. It also reveals phase-pure BaSnO₃ (001) within resolution of XRD, with an expanded out-of-plane lattice parameter of $4.127 \text{ \AA} \pm 0.001 \text{ \AA}$, which is about 0.26% larger than the bulk value of 4.116 \AA . The increased lattice parameter could result from a small amount of residual strain, cation nonstoichiometry, and/or other structural defects. To examine the influence of strain, a similar thickness of BaSnO₃ film was grown on a LaAlO₃ (001) substrate under identical growth conditions. LaAlO₃ substrates offer a larger lattice mismatch, and therefore, films grown on LaAlO₃ are expected to achieve full strain relaxation compared to films of similar thicknesses grown on SrTiO₃. A WAXRD scan is shown in Fig. 3(b) for a 34-nm BaSnO₃ film grown on LaAlO₃ (001) substrate yielding an out-of-plane lattice parameter value of $4.116 \text{ \AA} \pm 0.001 \text{ \AA}$. This value is identical to the bulk value, suggesting that the expanded out-of-plane lattice parameter of the film on SrTiO₃ is likely due to an incomplete strain relaxation. We confirmed these results using asymmetric x-ray scans.

Figures 4(a) and 4(b) show off-axis RSMs taken around (103) reflection peak of the films grown on SrTiO₃ (001) and LaAlO₃ (001), respectively. The RSM of a 40-nm-thick film on SrTiO₃ shows an out-of-plane lattice parameter value of

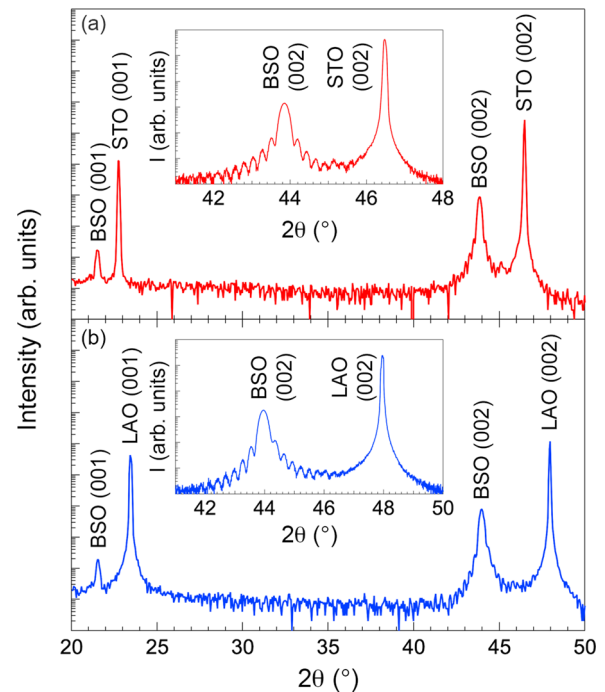


FIG. 3. (Color online) On-axis high-resolution x-ray diffraction 2θ - ω scans for (a) 40-nm BaSnO₃ (BSO) on STO (001), and (b) 34-nm BaSnO₃ on LAO (001) substrate. Insets show close-ups along (002) film/substrate peaks. The out-of-plane lattice parameter was calculated to be $4.127 \pm 0.001 \text{ \AA}$ and $4.116 \pm 0.001 \text{ \AA}$ for films grown on SrTiO₃ and LaAlO₃, respectively. Films were grown at identical growth conditions: $T_{\text{sub}} = 900 \text{ }^\circ\text{C}$, $P_{\text{HMDT}} = 1.3 \times 10^{-6} \text{ Torr}$, $P_{\text{Ba}} = 5.0 \times 10^{-8} \text{ Torr}$, and $P_{\text{ox}} = 5.0 \times 10^{-6} \text{ Torr}$.

$4.127 \pm 0.001 \text{ \AA}$, consistent with the results of on-axis WAXRD scans, and an in-plane lattice parameter value of $4.100 \pm 0.001 \text{ \AA}$. We calculate the unstrained film lattice parameter of BaSnO_3 using the following equation:⁴¹

$$a_{\text{unstrained}} = \frac{2\nu a_{\parallel} + (1-\nu)a_{\perp}}{1+\nu},$$

where ν is the Poisson's ratio for bulk BaSnO_3 [set to 0.247 (Ref. 42)], and a_{\parallel} and a_{\perp} are the experimental values of the in-plane and the out-of-plane lattice parameters, respectively, determined from the RSM. The value of $a_{\text{unstrained}}$ was calculated to be $4.116 \text{ \AA} \pm 0.001 \text{ \AA}$, which is identical to the bulk value, consistent with a stoichiometric film composition. Likewise, the film on LaAlO_3 was found to be fully relaxed [see Fig. 4(b)] with $a_{\text{unstrained}} = 4.116 \text{ \AA} \pm 0.001 \text{ \AA}$, as would be expected in stoichiometric films. These results thus further support our conclusion that films grown on both substrates are nearly stoichiometric.

To investigate structural defects arising from strain relaxation, cross-sectional STEM imaging and spectroscopy were performed. Figure 5(a) shows a low-magnification high-angle ADF (HAADF) STEM image of a 40-nm-thick

BaSnO_3 film on SrTiO_3 (001). Important features of this image are uniform film thickness over a large lateral length scale, a sharp film/substrate interface, and evenly spaced regions of different contrast with a spacing of $\sim 15 \text{ nm}$. We attribute the HAADF contrast to the complex defect regions propagating through the film from misfit dislocations, leading to slightly preferential milling during STEM sample preparation. The thickness contrast was also observed in the EELS map [see Fig. 5(d)] corresponding to these regions. It should be noted that a spacing of 7.5 nm is expected if misfit dislocations are responsible for relaxing the full 5.12% lattice mismatch.⁴³ This spacing is consistent with strain contrast modulations at the interface [Fig. 5(d)]. The questions of how and why dislocations propagate in the growth direction despite an in-plane mismatch and why the defect regions span twice the misfit dislocation distance are however open and require further investigations. A detailed analysis is underway to identify the origin and the nature of such defects. Figure 5(b) shows an atomic-resolution HAADF-STEM image of BaSnO_3 on SrTiO_3 , confirming a cube-on-cube epitaxial relationship. STEM-EDX elemental maps were recorded over a large lateral length scale [see Fig.

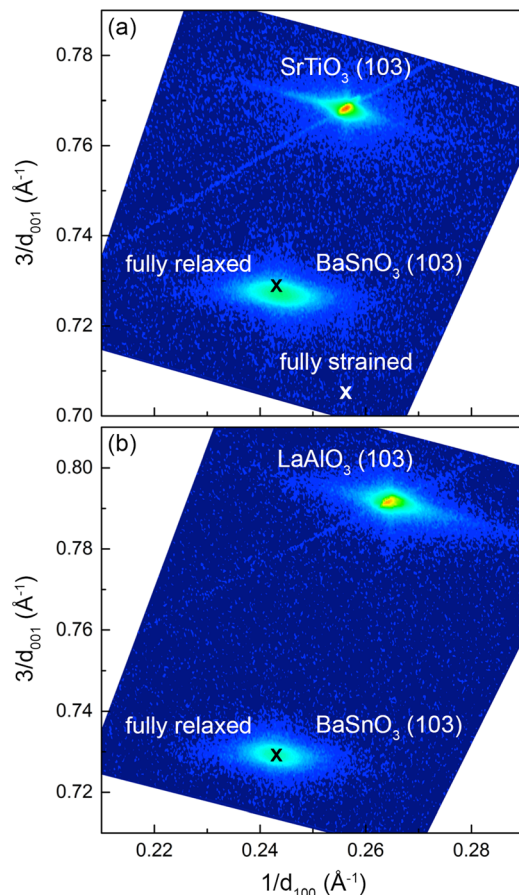


FIG. 4. (Color online) Off-axis RSMs of (a) 40-nm-thick BaSnO_3 film on SrTiO_3 , and (b) 34-nm-thick BaSnO_3 film on LaAlO_3 , taken around the (103)-reflection peak of the film. The film on SrTiO_3 was partially strained while the film on LaAlO_3 was completely relaxed. Black and white cross-markers show expected positions of a fully relaxed and a fully strained film, respectively. The marker for fully strained film on LaAlO_3 is not shown as it lies outside the field of view.

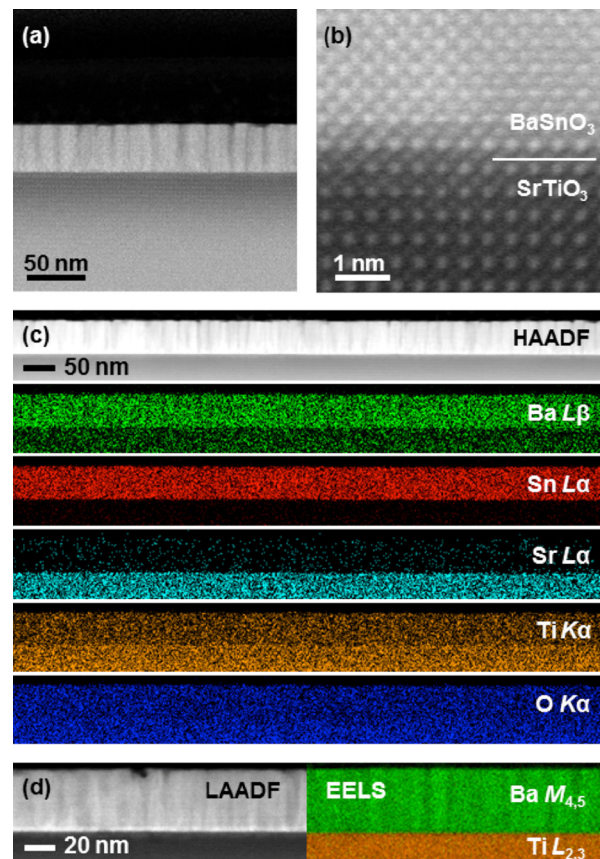


FIG. 5. (Color online) (a) HAADF-STEM image of a 40-nm-thick BaSnO_3 film on SrTiO_3 (001); (b) atomic-resolution HAADF-STEM image of a $\text{BaSnO}_3/\text{SrTiO}_3$ interface; (c) STEM-EDX maps of $\text{Ba } L_{\beta}$, $\text{Sn } L_{\alpha}$, $\text{Sr } L_{\alpha}$, $\text{Ti } K_{\alpha}$, and $\text{O } K_{\alpha}$ from a $\text{BaSnO}_3/\text{SrTiO}_3$ structure shown in the top panel. Poor contrast for Ba and Ti signal between film and the substrate is due to overlap of Ba and Ti x-ray peaks; (d) STEM-EELS composite map of $\text{Ba } M_{4,5}$ and $\text{Ti } L_{2,3}$ signals (right panel), collected along with a low-angle ADF (LAADF) STEM image (left panel).

5(c)], confirming uniform distribution of the elements in the film and no obvious signs of formation of different phases. It is noted that the poor contrast in Ba and Ti signals between film and substrate is due to overlap of Ba and Ti x-ray peaks. The STEM-EELS composite map [see Fig. 5(d)] for Ba $M_{4,5}$ and Ti $L_{2,3}$, however, confirms no obvious intermixing of Ba and Ti.

Finally, we attempt to discuss the role of HMDT chemistry in assisting the MBE growth of BaSnO₃, using a previously explored tin source (TET) as a reference [see Fig. S2 (Ref. 30)]. Application of HMDT results in the growth of stoichiometric BaSnO₃, while TET does not, despite the similar vapor pressures and thermal stabilities of the two chemicals [see Fig. S2 (Ref. 30)]. These precursors differ in two important aspects—the mass (and number of C–C bonds) of the alkyl group attached to Sn and the presence of a Sn–Sn bond in HMDT. The thermal dissociation energy of the Sn–Sn bond (146.7 kJ/mol)⁴⁴ in HMDT is reported to be smaller than that of Sn–C bonds (199.7 kJ/mol) in TET.⁴⁴ Additionally, based on the fact that TET is attached to bulkier C₂H₅ groups (cf. the CH₃-groups present in HMDT), one would expect the reactivity of HMDT to be higher than TET, as observed in our experiments. The striking divergence in growth performance displayed by these two chemicals demonstrates the vital role that precursor chemistry plays in the incorporation of tin, even at the elevated temperatures used in MBE. Future investigations should be directed toward investigating the reaction mechanisms involved in tin incorporation using HMDT, TET, and perhaps other similar precursors of tin, which may allow us to potentially design novel precursors for elements that are ordinarily difficult to oxidize.

IV. SUMMARY

In summary, we have demonstrated the growth of epitaxial, phase-pure, stoichiometric BaSnO₃ films via hybrid MBE using HMDT for tin, elemental source for Ba, and an rf plasma for oxygen plasma. Phase-pure films were also grown with molecular oxygen owing to high reactivity of HMDT. We illustrated using *in situ* RHEED that films grow in a layer-by-layer growth fashion and have a critical thickness of ~1 nm when grown on SrTiO₃. Phase purity, cation stoichiometry, surface morphology, and film microstructure were investigated using a combination of high-resolution x-ray diffraction, AFM, STEM imaging, and spectroscopy techniques. Future studies are underway to determine the extent of residual carbon concentration from the metalorganic precursor and to investigate the MBE “growth window”²³ for BaSnO₃. Finally, we argue that with a carefully selected/designed chemical precursor, MBE growth of complex oxides of elements possessing low vapor pressure and low oxidation potential may become possible, which are otherwise difficult to grow in a conventional MBE setup.

ACKNOWLEDGMENTS

The authors would like to acknowledge Dr. C. Leighton and Dr. W. L. Gladfelter for helpful discussion, Dr. G.

Haugstad for help with RBS measurements, and J. Halverson, K. Ganguly, T. Wang, and P. Xu for the technical help. This work was supported primarily through the U.S. National Science Foundation under Award No. DMR-1410888 and in part by NSF MRSEC under Award No. DMR-1420013. H.Y. acknowledges a fellowship from the Samsung Scholarship Foundation, Republic of Korea. Part of this work was carried out in the College of Science and Engineering Characterization Facility, and Minnesota Nano Center, University of Minnesota, which has received capital equipment funding from the NSF through the UMN MRSEC Program.

¹M. Schreyer and M. Jansen, *Angew. Chem. Int. Ed.* **114**, 665 (2002).

²A. Wold and K. Dwight, *J. Solid State Chem.* **88**, 229 (1990).

³D. Galusek and K. Ghillányová, *Ceramics Science and Technology* (Wiley-VCH Verlag GmbH & Co. KGaA, New York, 2010), p. 1.

⁴J. Livage, *J. Solid State Chem.* **64**, 322 (1986).

⁵J. Livage, M. Henry, and C. Sanchez, *Prog. Solid State Chem.* **18**, 259 (1988).

⁶S. J. May, A. B. Shah, S. G. E. T. Velthuis, M. R. Fitzsimmons, J. M. Zuo, X. Zhai, J. N. Eckstein, S. D. Bader, and A. Bhattacharya, *Phys. Rev. B* **77**, 174409 (2008).

⁷D. G. Schlom, A. F. Marshall, J. T. Sizemore, Z. J. Chen, J. N. Eckstein, I. Bozovic, and K. E. V. Dessonneck, *J. Cryst. Growth* **102**, 361 (1990).

⁸C. D. Theis and D. G. Schlom, *J. Cryst. Growth* **174**, 473 (1997).

⁹B. R. Johnson *et al.*, *Appl. Phys. Lett.* **56**, 1911 (1990).

¹⁰J. F. Ihlefeld *et al.*, *Appl. Phys. Lett.* **91**, 071922 (2007).

¹¹J. N. Eckstein and I. Bozovic, *Annu. Rev. Mater. Sci.* **25**, 679 (1995).

¹²S. B. Bhaduri, *Ceramics and Composites Processing Methods* (Wiley, New York, 2012), p. 391.

¹³P. Vanyssek, *CRC Handbook of Chemistry and Physics* (CRC, Boca Raton, FL, 2015), Vol. 96 [Online], pp. 5–80.

¹⁴H. Gamsjäger, J. Bugajski, T. Gajda, R. J. Lemire, and W. Preis, *Chemical Thermodynamics of Nickel* (Elsevier, France, 2005).

¹⁵L. Feigl, B. D. Schultz, S. Ohya, D. G. Ouellette, A. Kozhanov, and C. J. Palmström, *J. Cryst. Growth* **366**, 51 (2013).

¹⁶M. E. White, M. Y. Tsai, F. Wu, and J. S. Speck, *J. Vac. Sci. Technol. A* **26**, 1300 (2008).

¹⁷A. El-Shaer, A. C. Mofor, A. Bakin, M. Kreye, and A. Waag, *Superlattices Microstruct.* **38**, 265 (2005).

¹⁸Y. S. Kim, N. Bansal, and S. Oh, *J. Vac. Sci. Technol. A* **28**, 600 (2010).

¹⁹E. S. Hellman and E. H. Hartford, *J. Vac. Sci. Technol. B* **12**, 1178 (1994).

²⁰C. D. Theis and D. G. Schlom, *J. Vac. Sci. Technol. A* **14**, 2677 (1996).

²¹B. Jalan, R. Engel-Herbert, N. J. Wright, and S. Stemmer, *J. Vac. Sci. Technol. A* **27**, 461 (2009).

²²T. Wang, K. Ganguly, P. Marshall, P. Xu, and B. Jalan, *Appl. Phys. Lett.* **103**, 212904 (2013).

²³B. Jalan, P. Moetakef, and S. Stemmer, *Appl. Phys. Lett.* **95**, 032906 (2009).

²⁴Y. Matsubara, K. S. Takahashi, Y. Tokura, and M. Kawasaki, *Appl. Phys. Express* **7**, 125502 (2014).

²⁵P. Moetakef, D. G. Ouellette, J. Y. Zhang, T. A. Cain, S. J. Allen, and S. Stemmer, *J. Cryst. Growth* **355**, 166 (2012).

²⁶H. T. Zhang, L. R. Dedon, L. W. Martin, and R. Engel-Herbert, *Appl. Phys. Lett.* **106**, 233102 (2015).

²⁷J. A. Moyer, C. Eaton, and R. Engel-Herbert, *Adv. Mater.* **25**, 3578 (2013).

²⁸E. L. Mays, D. W. Hess, and W. S. Rees, Jr., *J. Cryst. Growth* **261**, 309 (2004).

²⁹T. Wang, A. Prakash, E. Warner, W. L. Gladfelter, and B. Jalan, *J. Vac. Sci. Technol. A* **33**, 020606 (2015).

³⁰See supplementary material at <http://dx.doi.org/10.1116/1.4933401> for x-ray diffraction of films grown with molecular oxygen, surface morphology, RHEED analysis for in-plane lattice parameter measurements, and the Rutherford backscattering study of films grown using HMDT and TET precursors.

³¹T. N. Stanislavchuk, A. A. Sirenko, A. P. Litvinchuk, X. Luo, and S. W. Cheong, *J. Appl. Phys.* **112**, 044108 (2012).

- ³²H. J. Kim *et al.*, *Phys. Rev. B* **86**, 165205 (2012).
- ³³H. J. Kim *et al.*, *Appl. Phys. Express* **5**, 061102 (2012).
- ³⁴M. Bjorck and G. Andersson, *J. Appl. Crystallogr.* **40**, 1174 (2007).
- ³⁵H. N. Yang, G. C. Wang, and T. M. Lu, *Phys. Rev. B* **51**, 17932 (1995).
- ³⁶R. Kunkel, B. Poelsema, L. K. Verheij, and G. Comsa, *Phys. Rev. Lett.* **65**, 733 (1990).
- ³⁷A. P. Kajdos and S. Stemmer, *Appl. Phys. Lett.* **105**, 191901 (2014).
- ³⁸W. Braun and K. Ploog, *Appl. Phys. A* **60**, 441 (1995).
- ³⁹D. J. Dunstan, S. Young, and R. H. Dixon, *J. Appl. Phys.* **70**, 3038 (1991).
- ⁴⁰J. W. Matthews and A. E. Blakeslee, *J. Cryst. Growth* **27**, 118 (1974).
- ⁴¹N. Goykhman, Y. Feldman, E. Wachtel, A. Yoffe, and I. Lubomirsky, *J. Electroceram.* **33**, 180 (2014).
- ⁴²E. Moreira, J. M. Henriques, D. L. Azevedo, E. W. S. Caetano, V. N. Freire, U. L. Fulco, and E. L. Albuquerque, *J. Appl. Phys.* **112**, 043703 (2012).
- ⁴³K. Ganguly, P. Ambwani, P. Xu, J. S. Jeong, K. A. Mkhoyan, C. Leighton, and B. Jalan, *APL Mater.* **3**, 062509 (2015).
- ⁴⁴A. K. Baev, *Russ. J. Phys. Chem.* **75**, 59 (2001).